CrossMark

Velocity Dispersion $\sigma_{\rm aper}$ Aperture Corrections as a Function of Galaxy Properties from Integral-field Stellar Kinematics of 10,000 MaNGA Galaxies

Kai Zhu[1,2,3] ⓘ, Ran Li[1,2,3] ⓘ, Xiaoyue Cao[1,2,3] ⓘ, Shengdong Lu[4,1], Michele Cappellari[5] ⓘ, and Shude Mao[4] ⓘ
[1] National Astronomical Observatories, Chinese Academy of Sciences, Beijing 100101, China; ranl@bao.ac.cn
[2] Institute for Frontiers in Astronomy and Astrophysics, Beijing Normal University, Beijing 102206, China
[3] School of Astronomy and Space Science, University of Chinese Academy of Sciences, Beijing 100049, China
[4] Department of Astronomy, Tsinghua University, Beijing 100084, China
[5] Sub-department of Astrophysics, Department of Physics, University of Oxford, Denys Wilkinson Building, Keble Road, Oxford, OX1 3RH, UK

Abstract

The second moment of the stellar velocity within the effective radius, denoted by $\sigma_{\rm e}^2$, is a crucial quantity in galaxy studies, as it provides insight into galaxy properties and their mass distributions. However, large spectroscopic surveys typically do not measure $\sigma_{\rm e}$ directly, instead providing $\sigma_{\rm aper}$, the second moment of the stellar velocity within a fixed fiber aperture. In this paper, we derive an empirical aperture correction formula, given by $\sigma_{\rm aper}/\sigma_{\rm e} = (R_{\rm aper}/R_{\rm e})^\alpha$, using spatially resolved stellar kinematics extracted from approximately 10,000 Sloan Digital Sky Survey–Mapping Nearby Galaxies at Apache Point Observatory integral field unit observations. Our analysis reveals a strong dependence of α on the *r*-band absolute magnitude $M_{\rm r}$, *g*–*i* color, and Sérsic index $n_{\rm Ser}$, where α values are lower for brighter, redder galaxies with higher Sérsic indices. Our results demonstrate that the aperture correction derived from previous literature on early-type galaxies cannot be applied to predict the aperture corrections for galaxies with intermediate Sérsic indices. We provide a lookup table of α values for different galaxy types, with parameters in the ranges of $-18 > M_{\rm r} > -24$, $0.4 < g$–$i < 1.6$, and $0 < n_{\rm Ser} < 8$. A Python script is provided to obtain the correction factors from the lookup table.

Key words: galaxies: evolution – galaxies: formation – galaxies: kinematics and dynamics – galaxies: structure

1. Introduction

Stellar kinematics provide crucial information for understanding the mass distributions of galaxies. The advent of integral field spectroscopy (IFS) surveys, such as the Spectroscopic Areal Unit for Research on Optical Nebulae (SAURON; de Zeeuw et al. 2002), ATLAS$^{\rm 3D}$ (Cappellari et al. 2011), Calar Alto Legacy Integral Field Area (CALIFA; Sánchez et al. 2012), Sydney/AAO Multi-object Integral-field spectrograph (SAMI; Bryant et al. 2015), and Mapping Nearby Galaxies at Apache Point Observatory (MaNGA; Bundy et al. 2015), has allowed for spatially resolved stellar kinematics, which, when combined with well-established dynamical modeling methods, such as Schwarzschild modeling (Schwarzschild 1979) and Jeans Anisotropic Modeling (JAM; Cappellari 2008, 2020), can provide accurate measurements of the mass distribution of galaxies (Cappellari et al. 2006, 2013; Scott et al. 2015; Li et al. 2018; Zhu et al. 2018, Zhu et al. 2023a). The scaling relations between the dynamical properties and the stellar populations of the galaxies can be explored in detail (e.g., Cappellari 2016; Li et al. 2018; Lu et al. 2023).

However, the high cost of obtaining spatially resolved kinematics limits the applicability of IFS to a significantly larger number of local galaxies, such as the millions of galaxies in the Sloan Digital Sky Survey (SDSS), or distant galaxies at high redshift that cannot be spatially resolved. Thus, the second moment of stellar velocity within an aperture $\sigma_{\rm aper}$, which is measured using single-fiber spectroscopy, remains a fundamental quantity for understanding the dynamics of galaxies. Important scaling relations, such as fundamental plane (Djorgovski & Davis 1987; Dressler et al. 1987; Jorgensen et al. 1995) and mass plane (e.g., Auger et al. 2010; Cappellari et al. 2013; Zhu et al. 2023b), are derived with respect to $\sigma_{\rm aper}$ as well. However, galaxies have different angular sizes spanning a wide dynamic range, but the fiber size is fixed. As a result, velocity moments are not measured coherently for the entire galaxy sample. Therefore, researchers need to correct the measured velocity dispersion to a physically meaningful radius, which is typically the effective radius of a galaxy (Auger et al. 2010; Chen et al. 2019; de Graaff et al. 2021).

Earlier studies on velocity dispersion aperture corrections focused on early-type galaxies, with velocity dispersion profiles typically described as a power-law function of the form shown in Equation (2). Jorgensen et al. (1995) derived a power-law slope of $\alpha = -0.04$ for the early-type galaxies in nine clusters, while Mehlert et al. (2003) found $\alpha = -0.063$ for 35 early-type galaxies in the Coma cluster. A later study based on the SAURON IFS data analyzed 40 early-type galaxies and

reported a slope of $\alpha = -0.066 \pm 0.035$ (Cappellari et al. 2006). The aperture corrections were extended to 300 CALIFA galaxies across the Hubble sequence (Falcón-Barroso et al. 2017), which found a consistent power-law slope for the early-type galaxies ($\alpha = -0.055 \pm 0.020$) and a strong variation of α with magnitude (or stellar mass) for the late-type galaxies ($\alpha = 0.047 \pm 0.021$ for $M_r < -22$, $\alpha = 0.086 \pm 0.013$ for $-22 < M_r < -20$, and $\alpha = 0.153 \pm 0.063$ for $M_r > -20$). Despite the α variation with magnitude, the non-negligible scatter in a given M_r bin (especially for the late-type galaxies of $M_r > -20$) indicates a potential secondary contributor to the variation of α. The unprecedently large sample of the MaNGA survey provides the ability to perform a further and more comprehensive analysis of the velocity dispersion aperture correction. Recently, de Graaff et al. (2021) derived $\alpha = -0.033 \pm 0.003$ from the MaNGA data, but they only selected a subset of MaNGA sample (702 galaxies).

In this work, we take advantage of the full sample ($\sim$10,000) of MaNGA IFS observations to perform a more detailed classification of galaxies and try to obtain more accurate aperture corrections for each type of galaxy. We investigate the relations between the shape of velocity dispersion profiles (quantified by a power-law form) and other properties, e.g., magnitude, color, and Sérsic index (Sersic 1968). By selecting galaxies within a narrow parameter range, we aim to eliminate the effect of sample bias and provide a lookup table that can be applied to various types of galaxies, resulting in more precise aperture corrections.

The organization of this paper is as follows. In Section 2, we provide a brief overview of the stellar kinematic data and the MaNGA sample. Our main results are presented in Section 3. Finally, we summarize our conclusions in Section 4. We adopt a standard cosmology with $\Omega_m = 0.3$, $\Omega_\Lambda = 0.7$, and $H_0 = 70 \, \text{km s}^{-1} \, \text{Mpc}^{-1}$ throughout this work.

2. Data

2.1. The MaNGA Survey

As a part of the SDSS-IV, the MaNGA (Bundy et al. 2015) is an integral field unit (IFU) survey that uses tightly packed arrays of optical fibers to obtain spectral measurements of approximately 10,000 nearby galaxies. Using the Baryon Oscillation Spectroscopic Survey spectrographs (Smee et al. 2013; Drory et al. 2015) on the Sloan 2.5 m telescope (Gunn et al. 2006) at the Apache Point Observatory, this survey covers a radial range up to 1.5 effective radii (R_e) for the primary+ sample and up to 2.5 R_e for the secondary sample (Law et al. 2015; Wake et al. 2017). MaNGA provides spatially resolved spectra with a spaxel size of 0.5″, and the average g-band point-spread function (PSF) FWHM throughout the survey is about 2.54″ (Law et al. 2016).

The spectral measurements across the wavelength range of 3600–10300 Å have a spectral resolution of $\sigma = 72 \, \text{km s}^{-1}$

(Law et al. 2016). The raw observational data require spectrophotometric calibration (Yan et al. 2016), which is performed using the Data Reduction Pipeline (DRP) (Law et al. 2016). The DRP processes the data to produce three-dimensional data cubes that can be used to create spatially resolved maps of the galaxies under observation.

2.2. Stellar Kinematics

The Data Analysis Pipeline (DAP; Belfiore et al. 2019; Westfall et al. 2019) is responsible for producing higher-level products, such as stellar kinematics, nebular emission-line properties, and spectral indices of galaxies. The stellar kinematic information is derived from the IFU spectra using the PPXF software (Cappellari & Emsellem 2004; Cappellari 2017, 2022), which fits absorption lines with a subset of the Medium resolution Isaac Newton Telescope Library of Empirical Spectra (MILES; Sánchez-Blázquez et al. 2006; Falcón-Barroso et al. 2011) stellar library, MILES-HC. The spectra are Voronoi binned (Cappellari & Copin 2003) to $S/N = 10$ to ensure the reliability of the derived stellar velocity dispersions, which are presented as a combination of the intrinsic velocity dispersion of stars (σ_*) and the quadrature difference between the instrumental dispersion of the galaxy template and the MaNGA data (σ_{diff}). The velocity dispersion of the galaxy can be obtained using the equation $\sigma_*^2 = \sigma_{\text{obs}}^2 - \sigma_{\text{diff}}^2$, where σ_{obs} is the observed velocity dispersion (Westfall et al. 2019). In this work, we make use of the maps of stellar velocity, stellar velocity dispersion, and g-band flux, which are taken from the DAP outputs[6].

2.3. Sample Selection

We obtain 10,735 DAP outputs from SDSS DR17 (Abdurro'uf & Aerts 2022), which includes 10,296 observations of galaxies and the ancillary program targets, such as the Coma, IC342, M31, and globular clusters. After excluding 151 flagged data cubes that have been identified as critical quality or unusual quality from 10,296 galaxy observations, there are 10,145 high-quality data cubes corresponding to 10,010 unique galaxies and 135 repeat observations. The sample has a nearly uniform distribution of stellar masses in the range of 10^9–$6 \times 10^{11} \, M_\odot$ and a median redshift of approximately 0.03 (Wake et al. 2017).

In this work, we use the stellar kinematics of 10,010 unique galaxies but remove the galaxies that have been identified as having bad stellar kinematics (Zhu et al. 2023a). Finally, we obtain a sample of 9132 galaxies. The distribution of the whole sample is presented in Figure 1, in which the color g–i, the r-band absolute magnitude M_r, and the Sérsic index are taken from the PyMorph catalog (Domínguez Sánchez et al. 2022). As shown in Figure 1, the sample spans a wide range of
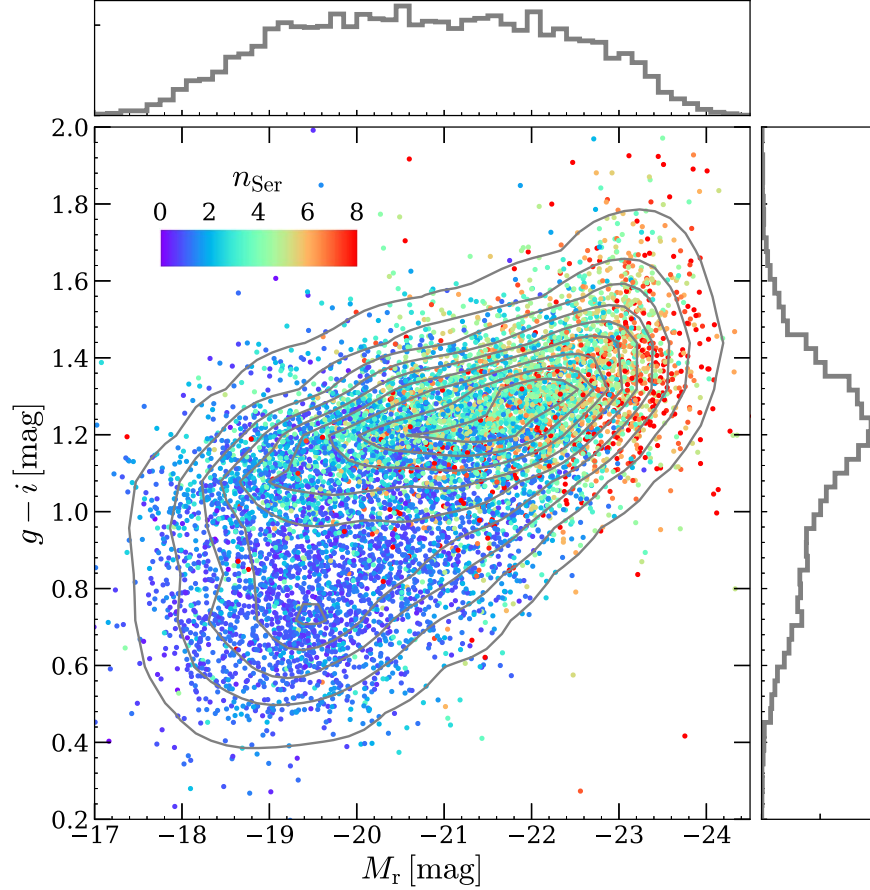
---

6 https://www.sdss.org/dr17/manga/manga-data/data-access/

Figure 1. Color–magnitude diagram, with symbols color-coded by the Sérsic index. All the quantities (r-band absolute magnitude, g–i color, and Sérsic index n_{Ser}) are taken from the PyMorph catalog (Domínguez Sánchez et al. 2022). The gray contours are the two-dimensional number density distributions, while the gray histograms on the top and right are the one-dimensional distributions (normalized to unity).

galactic properties: from the faint ($M_{\mathrm{r}} = -18$ mag) to the bright ($M_{\mathrm{r}} = -24$ mag) and from the blue (g–$i = 0.4$ mag) to the red (g–$i = 1.6$ mag). The large sample and various types of galaxies (i.e., the red sequence, the blue cloud, and the green valley) enable us to comprehensively study the aperture effects on the velocity dispersion.

3. Results

3.1. Integrated Stellar Velocity Dispersion Profiles

We derive the integrated stellar velocity dispersion within a set of apertures and obtain the aperture profiles for the whole sample. The integrated velocity dispersion is defined as the flux-weighted second velocity moments within a given elliptical aperture of area $A = \pi R_{\mathrm{aper}}^2$, written as

$$\sigma_{\mathrm{aper}} \approx \langle v_{\mathrm{rms}}^2 \rangle_{\mathrm{aper}}^{1/2} = \sqrt{\frac{\sum_k F_k (V_k^2 + \sigma_k^2)}{\sum_k F_k}}, \qquad (1)$$

where V_k, σ_k, and F_k are the stellar velocity, stellar velocity dispersion, and g-band flux in the kth spaxel, respectively. Following Cappellari et al. (2013, Section 3.3.3), we choose to use the elliptical aperture instead of the circular aperture to properly account for the inclination effects. Using elliptical apertures is also more appropriate for flat galaxies, which are typically dominated by rotation. If a circular aperture defined by the effective radius is used, the peak of rotation may be located outside the aperture, resulting in an underestimated σ_{aper}. Because the V and σ of DAP outputs are derived from the Voronoi binned spectra, we assign the binned values to each $0.5'' \times 0.5''$ spaxel belonging to each Voronoi bin. We calculate σ_{aper} within the elliptical apertures with fixed ellipticity and position angle (PA), which are derived from the single-component Sérsic fits (Domínguez Sánchez et al. 2022).

In Figure 2, we present an example to illustrate the calculation of integrated stellar velocity dispersion within a given elliptical aperture. In this figure, the pixels within the red ellipse of area $A = \pi R_{\mathrm{e}}^2$ are adopted to estimate the effective
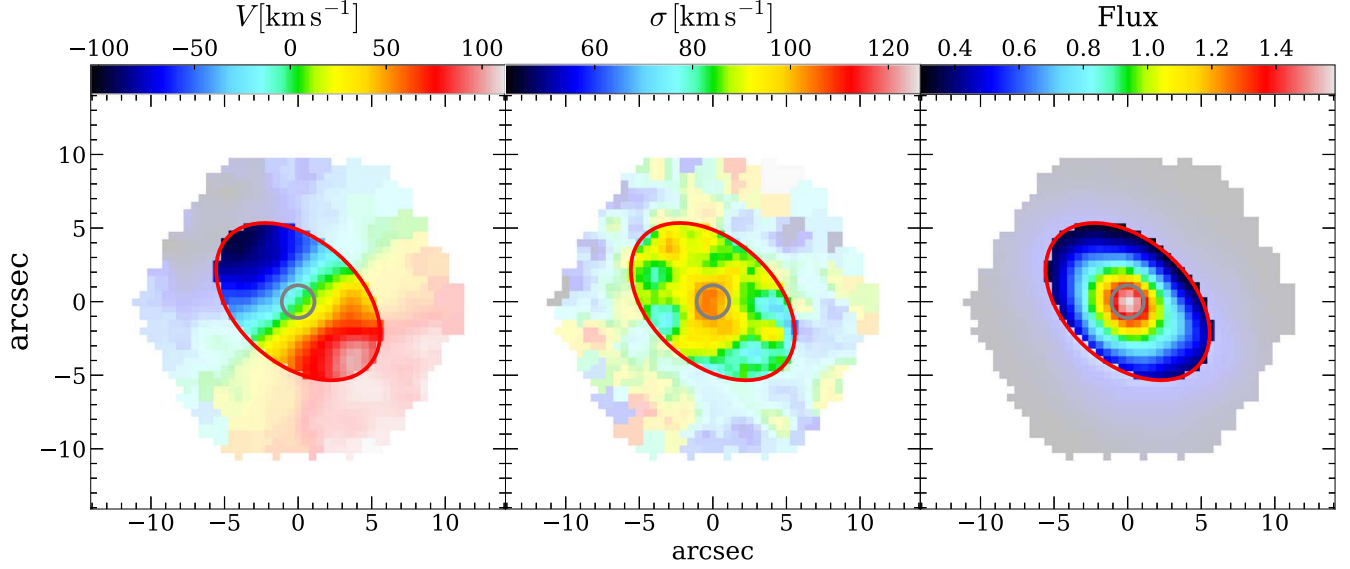
Figure 2. Illustration for the definition of σ_{aper} (MaNGA ID: 12-180432). The panels from left to right are the maps of stellar velocity, stellar velocity dispersion, and g-band flux. The gray circle denotes the $\mathrm{FWHM}_{\mathrm{PSF}}/2.355$, while the red ellipse is the half-light isophote of area $A = \pi R_e^2$, where R_e is the effective radius. The R_e, ellipticity, and PA are taken from the single Sérsic fits (Domínguez Sánchez et al. 2022). The σ_e is calculated using Equation (1) and the pixels within the red ellipse, while σ_{aper} values are determined within the concentric ellipses of area $A = \pi R_{\mathrm{aper}}^2$.

velocity dispersion σ_e using Equation (1). The effective velocity dispersion σ_e is demonstrated to agree well with that measured from a single fit on the stacked spectra within the same aperture (Cappellari et al. 2013). Moreover, we also calculate the integrated velocity dispersion within a circular aperture with a diameter of 3″, like the SDSS single fibers using Equation (1). Then, we match the galaxies with the spectroscopic catalog of SDSS DR8[7] (Aihara et al. 2011) and compare the velocity dispersion values obtained with two methods in Figure 3. To ensure that the velocity dispersions derived from the SDSS single-fiber spectra are reliable, we only select the spectral measurements with median $\mathrm{S/N} > 10$. As shown in Figure 3, we perform a linear fit to the two quantities with the LTS_LINEFIT[8] software (Cappellari et al. 2013), which combines the least-trimmed-squares robust technique of Rousseeuw & Driessen (2006) into a least-squares fitting algorithm and allows for the intrinsic scatter and errors in all coordinates. As shown in the figure, the slope ($b = 0.9784 \pm 0.0019$) and the small rms scatter ($\Delta = 11\,\mathrm{km\,s^{-1}}$) denote the high consistency between the two measurements, while most detected outliers are potential unreliable measurements with velocity dispersions below the resolution limit ($100\,\mathrm{km\,s^{-1}}$) of the SDSS spectrograph. This justifies the accuracy of Equation (1) in estimating the integrated stellar velocity dispersion within a given aperture from the IFU kinematics.
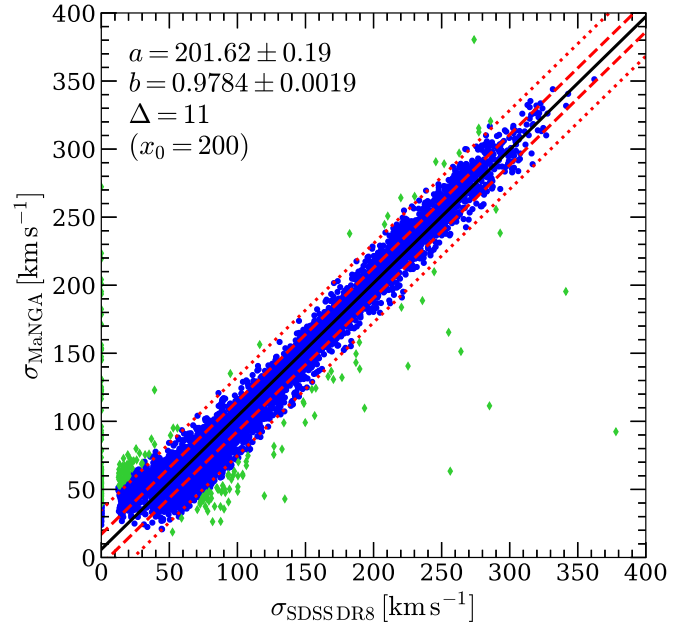

Figure 3. Comparison of the stellar velocity dispersion derived from the MaNGA survey with the SDSS DR8 measurements (Aihara et al. 2011) within the same circular aperture of 3″ diameter. The velocity dispersions of MaNGA are computed using Equation (1), while those from SDSS DR8 are from the single fit of the integrated spectra with the same aperture. The black solid, red dashed, and red dotted lines are the best-fitting, 1σ, and 2.6σ lines obtained using the LTS_LINEFIT procedure (with clip=3). The coefficients of the best-fitting $y = a + b \times (x - x_0)$ are shown in the panel, while Δ is the observed rms scatter. The green symbols are the detected outliers of LTS_LINEFIT beyond 3σ confidence level.
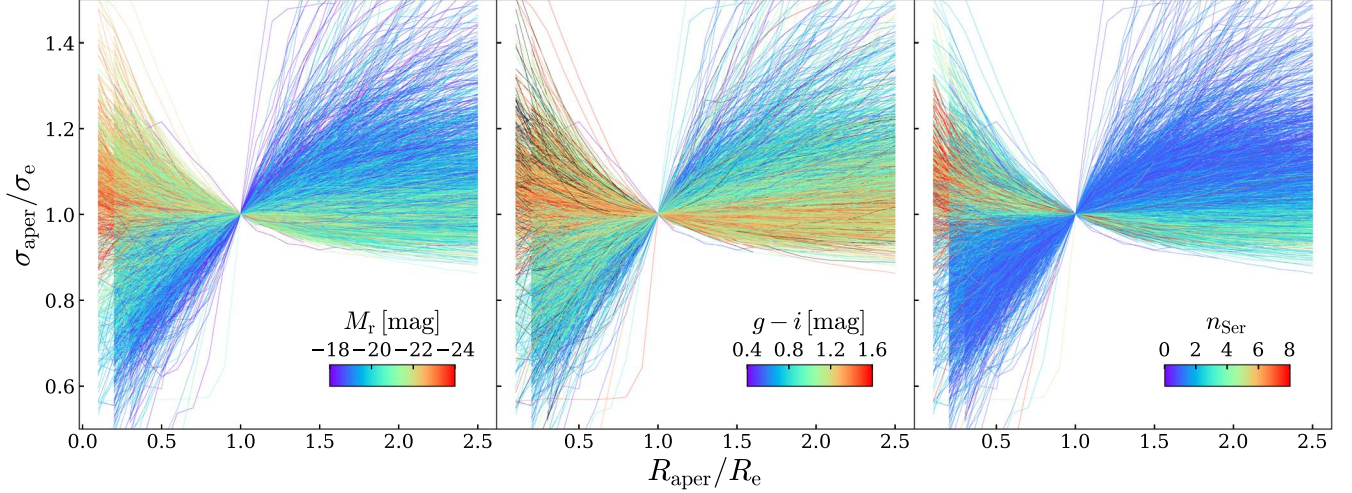

Figure 4. The stellar velocity dispersion integrated within elliptical apertures (the area equals πR_{aper}^2) as a function of radius. The profiles are normalized by the effective radius R_{e} and the dispersion σ_{e} within an elliptical aperture of area $A = \pi R_{\mathrm{e}}$. The profiles are colored by r-band absolute magnitude M_{r} (left), g–i color (middle), and Sérsic index n_{Ser} (right).
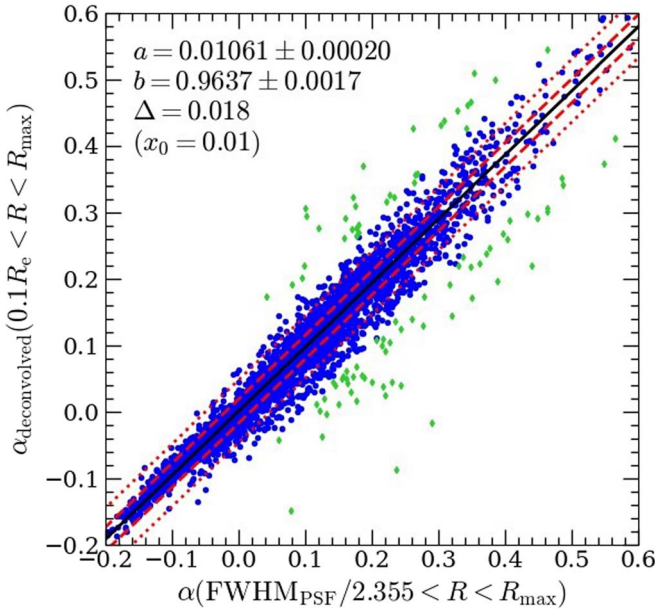

Figure 5. Comparison of the power-law index α from fitting within $\mathrm{FWHM_{PSF}}/2.355 < R < R_{\mathrm{max}}$ (Equation (3a)) with those deconvolved values fitting within $0.1R_{\mathrm{e}} < R < R_{\mathrm{max}}$. The deconvolved α values are obtained from convolving the MaNGA PSF on the model σ_{aper} profiles during the fitting process. The lines and symbols are the same as in Figure 3 but with a `clip=5` in the LTS_LINEFIT fitting, which means that the green symbols are the outliers beyond 5σ confidence level.

For each galaxy, we calculate the σ_{aper} within a set of elliptical apertures of area $A = \pi R_{\mathrm{aper}}^2$. R_{aper} ranges from $0.1R_{\mathrm{e}}$ to $2.5R_{\mathrm{e}}$, with a linear step of $0.1R_{\mathrm{e}}$. We use the R_{e} and the effective velocity dispersion σ_{e} as normalization factors to rescale the integrated velocity dispersion profiles. The normalized profiles are presented in Figure 4, which are colored by the

SDSS r-band (Stoughton et al. 2002) absolute magnitude M_{r} (left panel), the color g–i (middle panel), and the Sérsic index n_{Ser} (right panel). As can be seen, the σ_{aper} profiles vary significantly with different galactic properties: the brighter and redder galaxies with higher Sérsic index tend to have decreasing σ_{aper} profiles, while the fainter and bluer galaxies with lower Sérsic index show increasing trends toward outside. The increasing (decreasing) trends of σ_{aper} profiles are due to their different V/σ profiles. The σ_{aper} of massive and red galaxies with higher Sérsic index tend to be dispersion dominated and the dispersions decrease with increasing radius, while the less massive and blue galaxies are rotation supported and the σ_{aper} profiles increase in tandem with rotation curves.

The dependencies of σ_{aper} profiles on other galactic properties are consistent with the large variations of σ_{aper} profiles across a wide range of morphological types observed in Falcón-Barroso et al. (2017), which analyzed the σ_{aper} profiles for 300 CALIFA galaxies (Sánchez et al. 2012). However, the significantly larger sample (approximately 10,000 galaxies) of MaNGA enables a more detailed analysis and provides more accurate aperture corrections for integrated velocity dispersion measurements for specific types of galaxies.

3.2. Slopes of σ_{aper} Profiles for Different Types of Galaxies

Following previous works in the literature (Jorgensen et al. 1995; Cappellari et al. 2006; Falcón-Barroso et al. 2017), we use a power-law function to quantify the slopes of the normalized σ_{aper} profiles as

$$\left(\frac{\sigma_{\mathrm{aper}}}{\sigma_{\mathrm{e}}}\right) = \left(\frac{R_{\mathrm{aper}}}{R_{\mathrm{e}}}\right)^{\alpha}. \qquad (2)$$
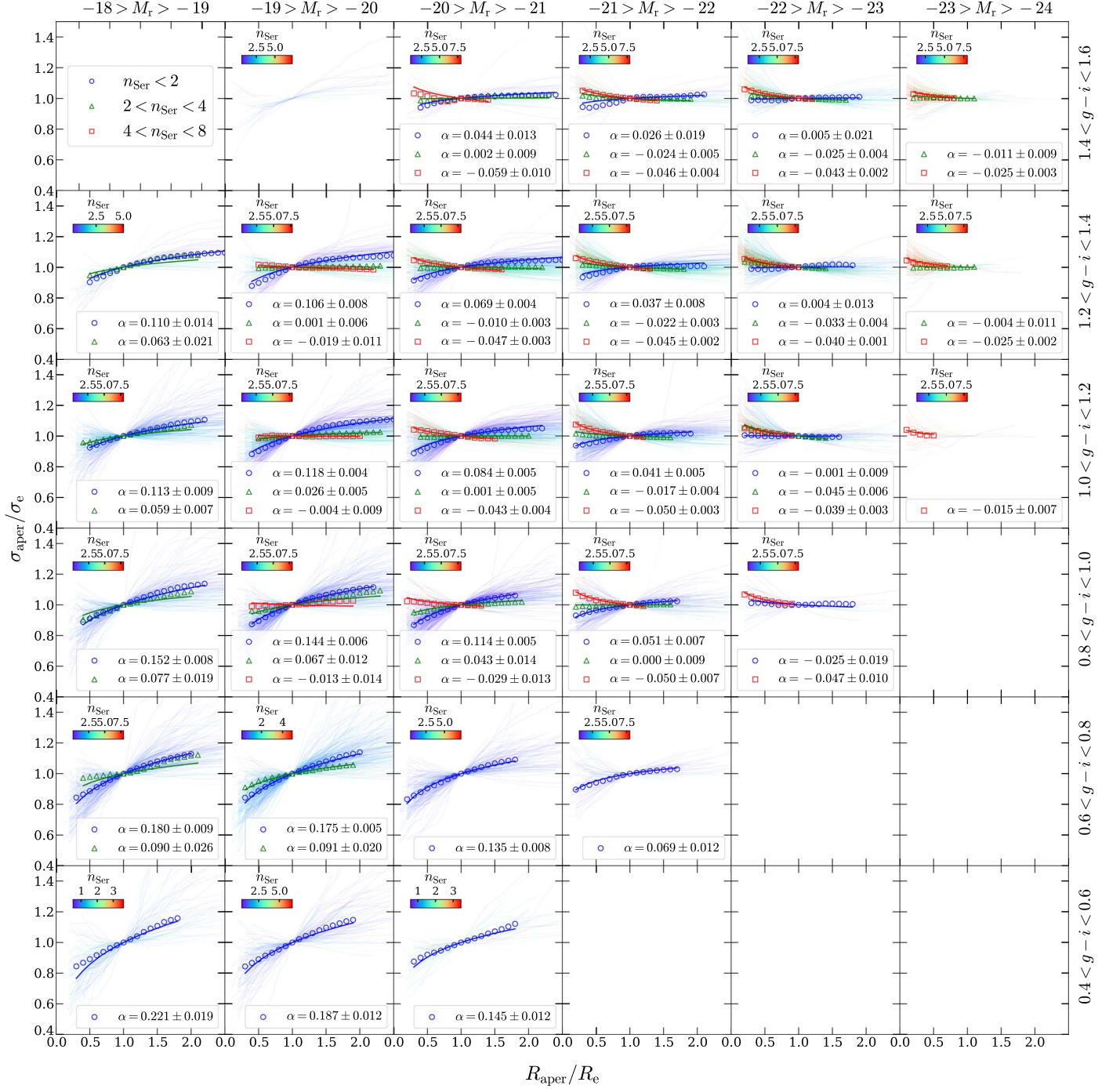
Figure 6. Normalized integrated velocity dispersion profiles in different M_r and g–i bins, where M_r is the r-band absolute magnitude and g–i color is the difference between g-band and i-band absolute magnitudes. The $\sigma_{\rm aper}$ profiles are colored by the Sérsic index $n_{\rm Ser}$. In each panel within a given ($M_{\rm aper}$, g–i) bin, the biweight mean profiles for different $n_{\rm Ser}$ are shown as blue circles ($n_{\rm Ser} < 2$), green triangles ($2 < n_{\rm Ser} < 4$), and red squares ($4 < n_{\rm Ser} < 8$). The mean and standard deviation of α (see the text at the bottom of panels) for each subset of galaxies (at least 15) are obtained from bootstrapping with 100 iterations. The curves (blue, green, and red) overlaid on the symbols are the corresponding modeled $\sigma_{\rm aper}$ profiles, which are described in the form of a power-law function (Equation (2)).

We fit the individual $\sigma_{\rm aper}$ profiles for each galaxy within a range of $[R_{\rm in}, R_{\rm out}]$ defined as

$$R_{\rm in} = \max({\rm FWHM}/2.355, 0.1R_{\rm e}), \qquad (3a)$$

$$R_{\rm out} = \min(R_{\rm max}, 2.5R_{\rm e}), \qquad (3b)$$

where the FWHM is in g-band (from DAP), and $R_{\rm max}$ is the largest radius of Voronoi bins, to avoid the PSF effects on the

Table 1
Lookup Table for the Aperture Correction Factors of Integrated Stellar Velocity Dispersion

		M_r						n_{Ser}
		$[-19, -18]$	$[-20, -19]$	$[-21, -20]$	$[-22, -21]$	$[-23, -22]$	$[-24, -23]$	
$g-i$	$[1.4, 1.6]$	⋯	⋯	0.044 ± 0.013	0.026 ± 0.019	0.005 ± 0.021	⋯	$[0, 2]$
		⋯	⋯	0.002 ± 0.009	-0.024 ± 0.005	-0.025 ± 0.004	-0.011 ± 0.009	$[2, 4]$
		⋯	⋯	-0.059 ± 0.010	-0.046 ± 0.004	-0.043 ± 0.002	-0.025 ± 0.003	$[4, 8]$
	$[1.2, 1.4]$	0.110 ± 0.014	0.106 ± 0.008	0.069 ± 0.004	0.037 ± 0.008	0.004 ± 0.013	⋯	$[0, 2]$
		0.063 ± 0.021	0.001 ± 0.006	-0.010 ± 0.003	-0.022 ± 0.003	-0.033 ± 0.004	-0.004 ± 0.011	$[2, 4]$
		⋯	-0.019 ± 0.011	-0.047 ± 0.003	-0.045 ± 0.002	-0.040 ± 0.001	-0.025 ± 0.002	$[4, 8]$
	$[1.0, 1.2]$	0.113 ± 0.009	0.118 ± 0.004	0.084 ± 0.005	0.041 ± 0.005	-0.001 ± 0.009	⋯	$[0, 2]$
		0.059 ± 0.007	0.026 ± 0.005	0.001 ± 0.005	-0.017 ± 0.004	-0.045 ± 0.006	⋯	$[2, 4]$
		⋯	-0.004 ± 0.009	-0.043 ± 0.004	-0.050 ± 0.003	-0.039 ± 0.003	-0.015 ± 0.007	$[4, 8]$
	$[0.8, 1.0]$	0.152 ± 0.008	0.144 ± 0.006	0.114 ± 0.005	0.051 ± 0.007	-0.025 ± 0.019	⋯	$[0, 2]$
		0.077 ± 0.019	0.067 ± 0.012	0.043 ± 0.014	0.000 ± 0.009	⋯	⋯	$[2, 4]$
		⋯	-0.013 ± 0.014	-0.029 ± 0.013	-0.050 ± 0.007	-0.047 ± 0.010	⋯	$[4, 8]$
	$[0.6, 0.8]$	0.180 ± 0.009	0.175 ± 0.005	0.135 ± 0.008	0.069 ± 0.012	⋯	⋯	$[0, 2]$
		0.090 ± 0.026	0.091 ± 0.020	⋯	⋯	⋯	⋯	$[2, 4]$
		⋯	⋯	⋯	⋯	⋯	⋯	$[4, 8]$
	$[0.4, 0.6]$	0.221 ± 0.019	0.187 ± 0.012	0.145 ± 0.012	⋯	⋯	⋯	$[0, 2]$
		⋯	⋯	⋯	⋯	⋯	⋯	$[2, 4]$
		⋯	⋯	⋯	⋯	⋯	⋯	$[4, 8]$

Note. The galaxies are divided into six bins in r-band absolute magnitude M_r (for different columns), six bins in $g-i$ color (for different rows), and three bins in Sérsic index n_{Ser} (for different sub-rows). In total, there are 108 (M_r, $g-i$, n_{Ser}) bins. In each bin with a sample of at least 15 galaxies, the mean and standard deviation of α (see the definition in Equation (2)) are estimated from bootstrapping with 100 iterations. One also needs to account for the effect of aperture shape when applying the correction factors on the real observations with circular apertures (see discussion in Section 3.3).

determination of α parameters. As discussed in Section 6 of Falcón-Barroso et al. (2017), beam smearing may affect the integrated velocity dispersion at the very center of galaxies and lead to potential bias in measuring α parameters. However, we argue here that α will not be clearly affected because most data points of the σ_{aper} profiles are the integrated velocity dispersion within much larger apertures compared to the dispersion of PSF. Following Falcón-Barroso et al. (2017), we tried to convolve the MaNGA PSF to the model σ_{aper} profiles when fitting them to the observed ones. In Figure 5, we present the comparison between the α with PSF deconvolved (fitting in a range of $[0.1R_e, R_{max}]$) and the α with PSF un-deconvolved (fitting in a range of [FWHM/ 2.355, R_{max}]), and find the two values are in good agreement with a slope of 0.9637 ± 0.0017 and a small rms scatter of $\Delta = 0.018$ using the LTS_LINEFIT procedure. Practically, aperture correction is usually applied to correct the velocity second moment measured within a fiber aperture that is comparable to or even larger than the effective radius of the galaxy, to the effective radius. The PSF smearing effect at the inner region of the MaNGA data is not expected to introduce a significant bias to this correction. In our project, we did not include the PSF effect in our fiducial analysis.

We divide the full sample into different subsamples based on their r-band absolute magnitude M_r and $g-i$ color. There are six M_r bins ranging from -18 to -24 (from faint to bright) in a step of 1 mag and six bins of $g-i$ color from 0.4 to 1.6 (from blue to red). In Figure 6, we present the σ_{aper} profiles color-coded by Sérsic index, which still show large variations in a given narrow bin of (M_r, $g-i$). Thus, in each (M_r, $g-i$) bin, we further split the galaxies into different Sérsic index groups, i.e., $n_{Ser} < 2$, $2 < n_{Ser} < 4$, $4 < n_{Ser} < 8$. For each subsample (M_r, $g-i$, n_{Ser}) with at least 15 galaxies, we adopt the biweight (Hoaglin et al. 1983) mean value of α. The mean and standard deviation of α parameters (presented in each panel of Figure 6) are obtained from bootstrapping with 100 iterations. In each panel, the biweight mean σ_{aper} profiles with different Sérsic indices (denoted as blue circles, green triangles,
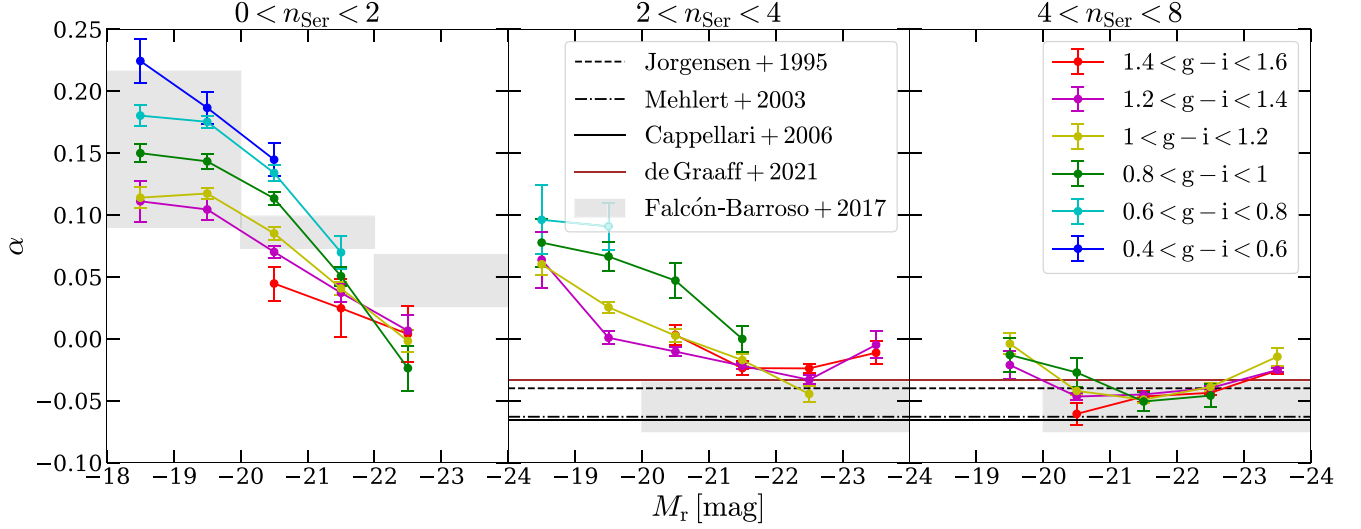
Figure 7. Power-law index α of integrated velocity dispersion profiles as a function of r-band absolute magnitude M_r for different g–i color (see the legends in the right panel) and Sérsic index n_{Ser} (see the top of each panel). The horizontal black dashed line is $\alpha = -0.04$ from Jorgensen et al. (1995), the horizontal black dashed–dotted line is $\alpha = -0.063$ from Mehlert et al. (2003), and the black solid line is $\alpha = -0.066$ from the SAURON project (Cappellari et al. 2006). The value of MaNGA subset (brown horizontal line), $\alpha = -0.033$, is taken from de Graaff et al. (2021), whose sample is dominated by the high Sérsic index galaxies but is not selected based on morphology. The gray-shaded squares are taken from the CALIFA survey (Falcón-Barroso et al. 2017), which derived α for both early-type and late-type galaxies.

and red squares) can be described well with the predicted power-law relations (solid lines) using the mean α values.

We create a lookup table[9] (Table 1) of aperture corrections for various types of galaxies by assuming a power-law function of σ_{aper} profiles. The table lists the mean and standard deviation of α, which are determined from bootstrapping with 100 iterations, for galaxies within given (M_r, g–i, n_{Ser}) bins.

In Figure 7, we investigate the relations between α parameters and M_r for galaxies with different g–i color and Sérsic index. Overall, the α values are smaller for brighter (smaller M_r), redder (higher g–i) galaxies with higher n_{Ser}. The smaller α parameters (i.e., the galaxies have larger central σ_{aper}) for galaxies with higher n_{Ser} are due to the fact that a larger n_{Ser} implies a greater concentration of central stellar mass, resulting in an increased central σ_{aper} and a steeper σ_{aper} profile.

The left panel of Figure 7 shows that for galaxies with $0 < n_{Ser} < 2$, which are typically classified as late-type galaxies, strong decreasing trends of α with increasing luminosity and redder color are observed. This suggests the importance of detailed classification when applying aperture corrections to late-type galaxies. The trend is consistent with the fact that redder spiral galaxies tend to host large bulges, resulting in increased central densities and larger central σ_{aper} values than their blue counterparts. It is worth noting that the variation in g–i color is responsible for the scatter of α in the

$-18 > M_r > -20$ bin, as compared to the α values of CALIFA late-type galaxies (Falcón-Barroso et al. 2017). In the brightest bin ($-22 > M_r > -24$), the α values of MaNGA late-type galaxies tend to be slightly smaller than those in Falcón-Barroso et al. (2017), likely due to the latter deriving values from galaxies with positive α instead of selecting galaxies based on Sérsic index or morphology.

Similar but weaker trends, where brighter and redder galaxies have smaller α, are also observed in the sample with $2 < n_{Ser} < 4$. However, for galaxies with $4 < n_{Ser} < 8$, they tend to have negative α values. In this bin, the α–M_r relation shows a flat U-shape, and the scatter among different color bins is small.

Our results for the $4 < n_{Ser} < 8$ bin are consistent with previous studies on early-type galaxies. For example, Jorgensen et al. (1995) found $\alpha = -0.04$, Mehlert et al. (2003) found $\alpha = -0.063$, SAURON (Cappellari et al. 2006, Section 2.3) found $\alpha = -0.066 \pm 0.035$, CALIFA (Falcón-Barroso et al. 2017, Section 6) found $\alpha = -0.055 \pm 0.020$, and a subset of MaNGA galaxies (de Graaff et al. 2021, Appendix C) found $\alpha = -0.033 \pm 0.003$. It should be noted that the subset of the MaNGA sample used in de Graaff et al. (2021) is dominated by galaxies with high Sérsic index but is not a pure early-type galaxy sample, so the α value for early-type galaxies is slightly shallower than what we found.

The results of this paper demonstrate that the aperture correction derived from previous literature on early-type galaxies cannot be applied to predict the aperture corrections

---

[9] A Python script is provided in https://github.com/kaizhu-astro/aperture_correction to obtain the correction factors from the lookup table.
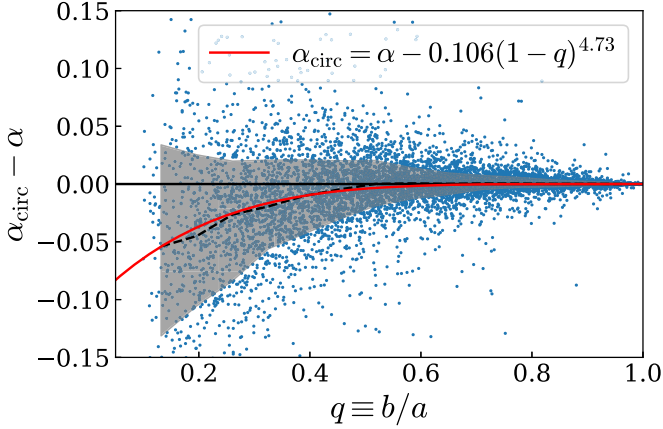
Figure 8. The $\alpha_{\rm circ} - \alpha$ as a function of axial ratio q. The α and $\alpha_{\rm circ}$ are derived from Equations (2) and (4), respectively, while the q is derived from Sérsic fits (Domínguez Sánchez et al. 2022). The black dashed curve and the gray-shaded region are the median value and [16th, 84th] percentiles. The red curve is the best-fitting empirical relation for all galaxies.

for galaxies with intermediate Sérsic indices, regardless of their color.

3.3. Corrections for the Velocity Dispersion Measured within a Circular Aperture

The clear trends that α varies with $M_{\rm r}$, g–i, and $n_{\rm Ser}$ highlight the enhanced accuracy of aperture corrections in this study. However, it is difficult to apply such aperture corrections in reality due to the fact of circular apertures in single-fiber observations. To further account for the effect of aperture shape, we also calculate the $\sigma_{\rm aper,\ circ}$, which is also defined as Equation (1) but within a circular aperture with a radius of $R_{\rm aper}$. We fit the $\sigma_{\rm aper,\ circ}$ profiles for each galaxy, which are normalized as

$$\frac{\sigma_{\rm aper,\ circ}}{\sigma_{\rm e}} = \left(\frac{R_{\rm aper}}{R_{\rm e}}\right)^{\alpha_{\rm circ}}, \qquad (4)$$

to obtain the power-law index $\alpha_{\rm circ}$. The $\alpha_{\rm circ}$ can be applied in real single-fiber observations to obtain the $\sigma_{\rm e}$.

In Figure 8, we show the $\alpha_{\rm circ} - \alpha$ as a function of axial ratio $q \equiv b/a$. As can be seen, the systematic difference between α and $\alpha_{\rm circ}$ is negligible for galaxies with $q > 0.4$, while flat galaxies ($q < 0.4$) tend to have smaller $\alpha_{\rm circ}$ than α. Given the small fraction ($\sim$20%) of galaxies with $q < 0.4$ in our sample, we do not present the $\alpha_{\rm circ}$ values in each ($M_{\rm r}$, g–i, $n_{\rm Ser}$), which are expected to be similar to α. As shown in the Appendix, similar trends can be seen if replacing α in Figure 7 with $\alpha_{\rm circ}$. However, we also found that the biweight mean $\sigma_{\rm aper,\ circ}/\sigma_{\rm e}$ profiles in some ($M_{\rm r}$, g–i, $n_{\rm Ser}$) bins cannot be well described by the function, especially for the $n_{\rm Ser} < 2$ galaxies that may suffer from strong inclination effects. This is likely due to the fact that the normalization of $\sigma_{\rm aper,\ circ}/\sigma_{\rm e}$ is nonphysical and will bring uncertainties when stacking the

normalized profiles in a given ($M_{\rm r}$, g–i, $n_{\rm Ser}$) bin. Thus, we choose to only present the α values and derive an empirical relation between α and $\alpha_{\rm circ}$, which relates to the axial ratio q in the form of

$$\alpha_{\rm circ} = \alpha - 0.106(1 - q)^{4.73}. \qquad (5)$$

One can use Table 1 to obtain α in a given ($M_{\rm r}$, g–i, $n_{\rm Ser}$) bin and then use Equation (5) to obtain the $\alpha_{\rm circ}$ if necessary ($q < 0.4$), but one should also be aware of the large scatter of ($\alpha_{\rm circ} - \alpha$) for very flat galaxies.

4. Conclusions

We conducted a comprehensive analysis of the aperture corrections for the integrated stellar velocity dispersion $\sigma_{\rm aper}$ using the full MaNGA sample. With a large sample size of approximately 10,000 galaxies, we were able to study aperture corrections in detail for a diverse range of galaxy types (Figure 1) for the first time. We derived the $\sigma_{\rm aper}$ profiles for the entire sample (Figure 4) and used a power-law function (Equation (2)) to quantify the profiles of different subsamples based on their r-band absolute magnitude $M_{\rm r}$, g–i color, and Sérsic index $n_{\rm Ser}$ (Figure 6). The relationships between the power-law index α and the three properties ($M_{\rm r}$, g–i, and $n_{\rm Ser}$) are presented in Table 1 and Figure 7.

Our analysis revealed several important findings regarding the aperture corrections of the integrated stellar velocity dispersion $\sigma_{\rm aper}$. First, we observed decreasing trends of the power-law index α with increasing $M_{\rm r}$, redder g–i color, and higher Sérsic index $n_{\rm Ser}$. While the α values of early-type galaxies with high $n_{\rm Ser}$ ($4 < n_{\rm Ser} < 8$) are consistent with previous studies in the literature, those of early-type galaxies with $2 < n_{\rm Ser} < 4$ cannot be predicted by models of previous studies. Second, we found that for late-type galaxies ($n_{\rm Ser} < 2$), the median α varies significantly with $M_{\rm r}$ and g–i color, with the largest variation in α on g–i color being up to $\sim$0.1 in $-19 < M_{\rm r} < -18$. These diverse α values and their clear correlations with other galactic properties highlight the importance of a comprehensive analysis based on the large sample of MaNGA.

In addition, we established an empirical relation between the power-law index α and $\alpha_{\rm circ}$, as shown in Equation (5). Here, $\alpha_{\rm circ}$ is defined as the power-law index derived from the velocity dispersion profile measured within circular apertures, which can be used to calculate $\sigma_{\rm e}$ for circular apertures with any given radius defined by the size of observational fiber. We believe that our findings will enable more precise aperture corrections for single-fiber spectroscopic survey, such as those from the SDSS and Dark Energy Spectroscopic Instrument survey. However, our empirical relations are derived from the MaNGA sample with a median redshift of $z = 0.03$, and some care should be taken when extrapolated to higher redshift galaxies. A possible solution could be using the higher redshift

IFS observations (e.g., Multi Unit Spectroscopic Explorer) to calibrate the relations.

Appendix
Tests on Using α_{circ} to Predict $\sigma_{\mathrm{aper,circ}}$ Profiles

We present two figures (Figures A1 and A2) that are similar to Figures 6 and 7, but σ_{aper} profiles and α are replaced with $\sigma_{\mathrm{aper,circ}}$ profiles and α_{circ}, respectively. We do not recommend directly using α_{circ} to predict $\sigma_{\mathrm{aper,circ}}$ profiles. See the text in Section 3.3 for a detailed discussion.
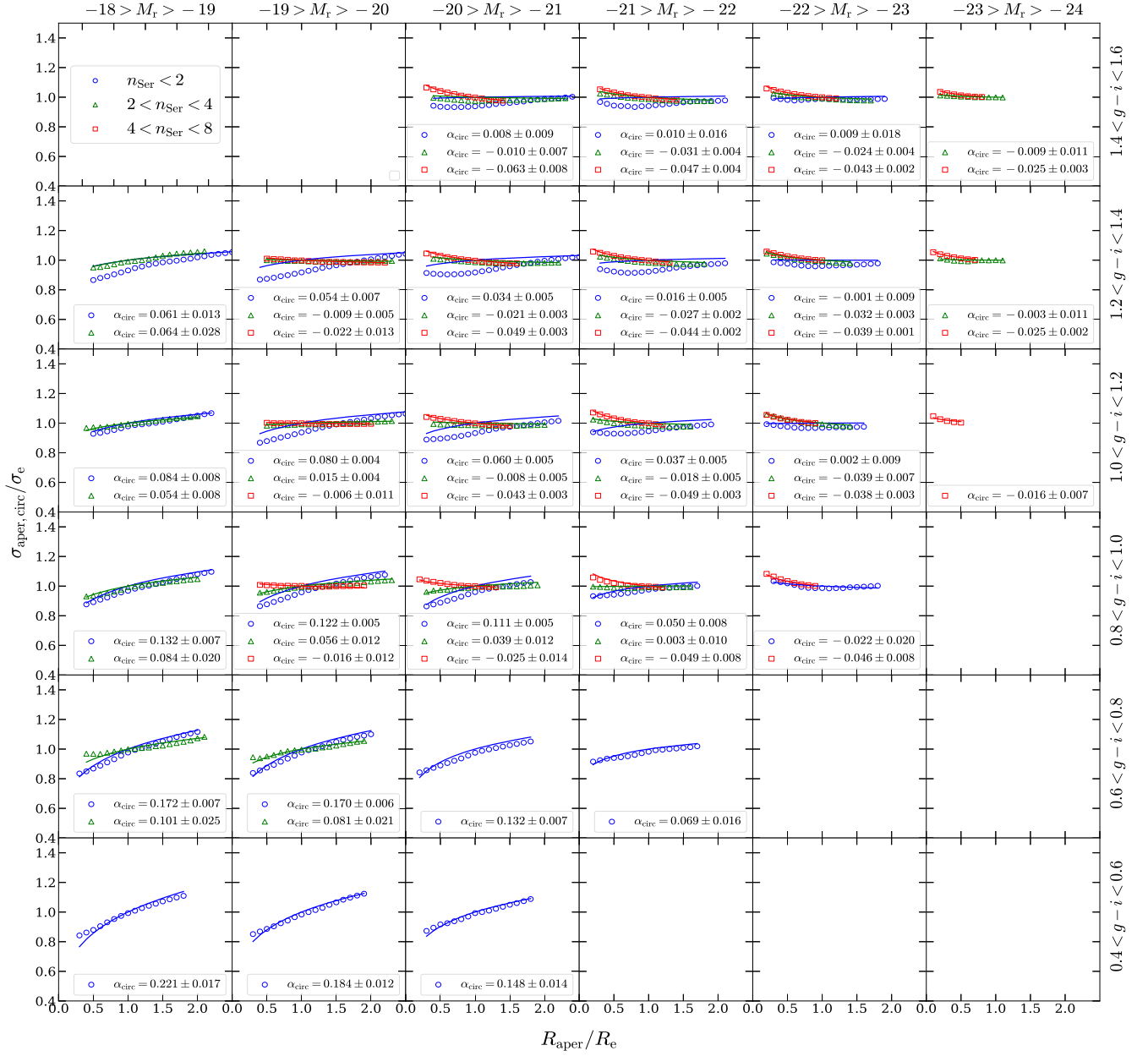
Figure A1. The same as Figure 6, but replacing σ_{aper} with $\sigma_{\text{aper,circ}}$.
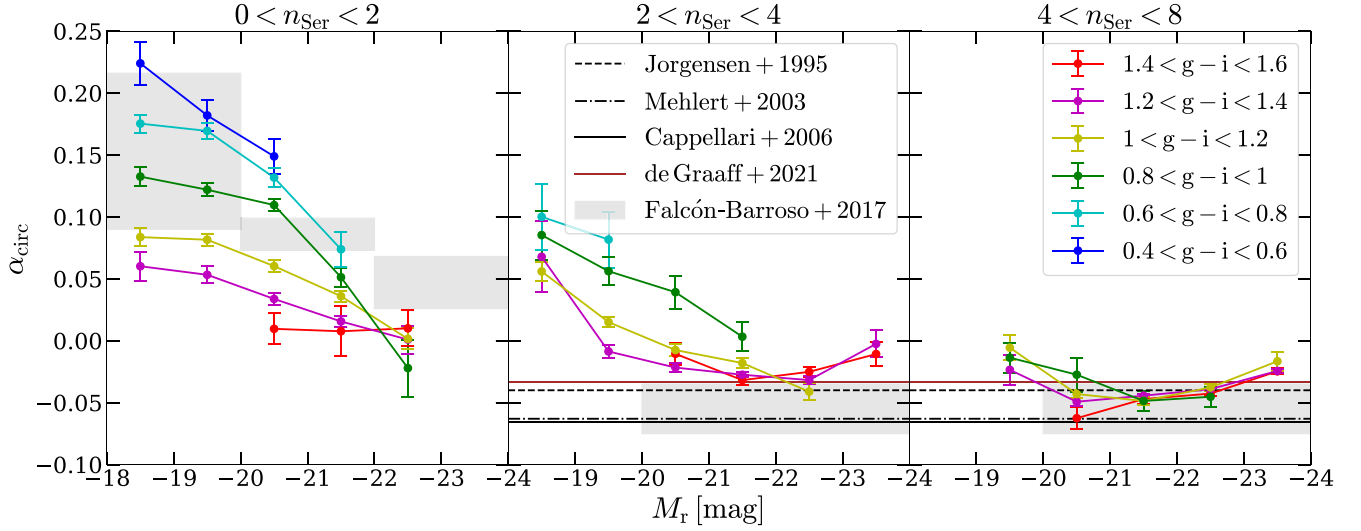
Figure A2. The same as Figure 7, but replacing α with α_{circ}.

ORCID iDs

Kai Zhu ⓘ https://orcid.org/0000-0002-2583-2669
Xiaoyue Cao ⓘ https://orcid.org/0000-0003-4988-9296
Shengdong Lu ⓘ https://orcid.org/0000-0002-6726-9499
Michele Cappellari ⓘ https://orcid.org/0000-0002-1283-8420
Shude Mao ⓘ https://orcid.org/0000-0001-8317-2788

References

Abdurro'uf, Accetta K., Aerts, C., et al. 2022, ApJS, 259, 35
Aihara, H., Allende Prieto, C., An, D., et al. 2011, ApJS, 193, 29
Auger, M. W., Treu, T., Bolton, A. S., et al. 2010, ApJ, 724, 511
Belfiore, F., Westfall, K. B., Schaefer, A., et al. 2019, AJ, 158, 160
Bryant, J. J., Owers, M. S., Robotham, A. S. G., et al. 2015, MNRAS, 447, 2857
Bundy, K., Bershady, M. A., Law, D. R., et al. 2015, ApJ, 798, 7
Cappellari, M. 2008, MNRAS, 390, 71
Cappellari, M. 2016, ARA&A, 54, 597
Cappellari, M. 2017, MNRAS, 466, 798
Cappellari, M. 2020, MNRAS, 494, 4819
Cappellari, M. 2022, arXiv:2208.14974
Cappellari, M., Bacon, R., Bureau, M., et al. 2006, MNRAS, 366, 1126
Cappellari, M., & Copin, Y. 2003, MNRAS, 342, 345
Cappellari, M., & Emsellem, E. 2004, PASP, 116, 138
Cappellari, M., Emsellem, E., Krajnović, D., et al. 2011, MNRAS, 413, 813
Cappellari, M., Scott, N., Alatalo, K., et al. 2013, MNRAS, 432, 1709
Chen, Y., Li, R., Shu, Y., & Cao, X. 2019, MNRAS, 488, 3745
de Graaff, A., Bezanson, R., Franx, M., et al. 2021, ApJ, 913, 103
de Zeeuw, P. T., Bureau, M., Emsellem, E., et al. 2002, MNRAS, 329, 513
Djorgovski, S., & Davis, M. 1987, ApJ, 313, 59

Domínguez Sánchez, H., Margalef, B., Bernardi, M., & Huertas-Company, M. 2022, MNRAS, 509, 4024
Dressler, A., Lynden-Bell, D., Burstein, D., et al. 1987, ApJ, 313, 42
Drory, N., MacDonald, N., Bershady, M. A., et al. 2015, AJ, 149, 77
Falcón-Barroso, J., Lyubenova, M., van de Ven, G., et al. 2017, A&A, 597, A48
Falcón-Barroso, J., Sánchez-Blázquez, P., Vazdekis, A., et al. 2011, A&A, 532, A95
Gunn, J. E., Siegmund, W. A., Mannery, E. J., et al. 2006, AJ, 131, 2332
Hoaglin, D. C., Mosteller, F., & Tukey, J. W. 1983, in Understanding Robust and Exploratory Data Anlysis Wiley Series in Probability and Mathematical Statistics, ed. D. C. Hoaglin, F. Mosteller, & J. W. Tukey (New York: Wiley)
Jorgensen, I., Franx, M., & Kjaergaard, P. 1995, MNRAS, 276, 1341
Law, D. R., Cherinka, B., Yan, R., et al. 2016, AJ, 152, 83
Law, D. R., Yan, R., Bershady, M. A., et al. 2015, AJ, 150, 19
Li, H., Mao, S., Cappellari, M., et al. 2018, MNRAS, 476, 1765
Lu, S., Zhu, K., Cappellari, M., et al. 2023, arXiv:2304.11712
Mehlert, D., Thomas, D., Saglia, R. P., Bender, R., & Wegner, G. 2003, A&A, 407, 423
Rousseeuw, P., & Driessen, K. 2006, Data Min. Knowl. Discov., 12, 29
Sánchez, S. F., Kennicutt, R. C., Gil de Paz, A., et al. 2012, A&A, 538, A8
Sánchez-Blázquez, P., Peletier, R. F., Jiménez-Vicente, J., et al. 2006, MNRAS, 371, 703
Schwarzschild, M. 1979, ApJ, 232, 236
Scott, N., Fogarty, L. M. R., Owers, M. S., et al. 2015, MNRAS, 451, 2723
Sersic, J. L. 1968, Atlas de Galaxias Australes (Córdoba: Obs. Astron. Univ. Nacional de Córdoba)
Smee, S. A., Gunn, J. E., Uomoto, A., et al. 2013, AJ, 146, 32
Stoughton, C., Lupton, R. H., Bernardi, M., et al. 2002, AJ, 123, 485
Wake, D. A., Bundy, K., Diamond-Stanic, A. M., et al. 2017, AJ, 154, 86
Westfall, K. B., Cappellari, M., Bershady, M. A., et al. 2019, AJ, 158, 231
Yan, R., Tremonti, C., Bershady, M. A., et al. 2016, AJ, 151, 8
Zhu, K., Lu, S., Cappellari, M., et al. 2023a, MNRAS, 522, 6326
Zhu, K., Lu, S., Cappellari, M., et al. 2023b, arXiv:2304.11714
Zhu, L., van de Ven, G., van den Bosch, R., et al. 2018, NatAs, 2, 233